Frontiers of Physics
https://doi.org/10.1007/s11467-021-1137-y
Front. Phys.
17(4), 42502 (2022)

RESEARCH ARTICLE

Simulation of EOM-based frequency-chirped laser slowing of MgF radicals

Kang Yan[1], RuoXi Gu[1], Di Wu[1], Jin Wei[1], Yong Xia[1,2,3,†], Jianping Yin[1,‡]

[1] *State Key Laboratory of Precision Spectroscopy, School of Physics and Electronic Science, East China Normal University, Shanghai 200241, China*
[2] *NYU-ECNU Institute of Physics at NYU Shanghai, Shanghai 200062, China*
[3] *Collaborative Innovation Center of Extreme Optics, Shanxi University, Taiyuan 030006, China*
Corresponding authors. E-mail: †yxia@phy.ecnu.edu.cn, ‡jpyin@phy.ecnu.edu.cn
Received October 23, 2021; accepted November 21, 2021

Here we propose a scheme to slow MgF molecules by using EOM-based frequency-chirped radiation pressure slowing. The scheme well addresses the need for a rapid chirp rate while light molecules are being laser slowed, whose scattering rate and recoil velocity are large. Two EOMs are used to compensate the rapidly changing Doppler shifts arised from the movement of molecules, and to cover the hyperfine energy structure of MgF, respectively. Based the scattering rate maps calculated from an optical Bloch equation model, individual molecule trajectories are simulated by using a semi-classical three-dimensional Monte Carlo approach. We show how the modulation configuration of EOM and the magnetic field influence the slowing results. The study shows that a cryogenic buffer gas-cooled MgF beam source is possible to be slowed down with a number of $\sim 1.4 \times 10^6$–10^7, and the final forward speed peaks at ~ 10 m/s near the capture velocity of a molecular MOT.

Keywords laser cooling of molecule, MgF molecule, laser slowing, dark state, type-II transition

1 Introduction

For decades, many efforts are made to produce ultracold molecules with large number and cold temperature [1, 2]. Such ultracold molecular species are increasingly being used for precision measurement of the electron's electric dipole moment [3, 4], ultracold chemistry [5, 6], complex quantum systems under precise control [7–10] and many-body physics [11–13]. Tremendous progress has been made in direct laser cooling and magneto-optical trap (MOT) of diatomic molecules, i.e., SrF [14, 15], YO [16, 17] and CaF [18], or even polyatomic molecules SrOH [19]. Furthermore, some species have been loaded into the magnetic trap [20] and dipole trap [21], then cooled to lower temperature by Sisyphus [22, 23], deep [24], collisional [25] and adiabatic-rapid-passage [26, 27] cooling, experimentally or theoretically. And other candidates, i.e., BaH [28], YbF [29], BaF [30–32], AlF [33] and MgF [34], are also in progress.

In order to be captured by an MOT, molecules must be slowed down below the capture velocity, typically 10–20 m/s [35–37], and laser radiation pressure slowing is a common method. It was first experimentally demonstrated in the deceleration of SrF with the frequency broadened slowing method, where a substantial flux of molecules with velocity < 50 m/s was obtained, showing the ability to scatter $> 10^4$ photons without heating the internal degrees of freedom of the molecules [38]. Based on the frequency broadened slowing, Hemmerling *et al.* applied "white-light" slowing and observed approximately 6×10^4 CaF molecules in a single pulse with velocities 10 ± 4 m/s [39]. On the other hand, frequency-chirped slowing was also demonstrated by Zhelyazkova *et al.* with CaF molecules being decelerated by about 20 m/s [40], and 7×10^5 CaF molecules per cm^2 per shot in a single rovibrational state with a velocity of 15 m/s was obtained by Truppe *et al.* [37]. Their experimental comparison between white-light and frequency-chirped slowing indicates that the chirped method gives far more molecules at lower speeds, e.g., about ten times more at 20 m/s. In addition, Yeo *et al.* used a combination of frequency-broadened and frequency-chirped slowing to generate a flux of YO below 10 m/s [41].

And other techniques, such as Zeeman slower bringing molecules to the desired forward speed at a specific position are also being developed and proposed by Petzold *et al.*. They first experimentally used this technique in K atom with molecule-like level structures [42]. Furthermore, Kaebert *et al.* investigated the feasibility of Zeeman slowing CaF molecules from a buffer-gas source, demonstrating that Zeeman slowing force is both strong and narrow [43].

Till now, frequency-chirped slowing is a mature tech-

* This article can also be found at http://journal.hep.com.cn/fop/EN/10.1007/s11467-021-1137-y.

nique with a brilliant performance. There is usually a chirp rate of dozens MHz/ms when directly chirping the carrier wave. However, it is far insufficient for slowing light molecules with a large recoil speed (such as a good candidate, MgF) because such chirp rate cannot well compensate the corresponding rapidly changing Doppler shifts. Thanks to the quick response of electric optical modulator (EOM) to the electric signal, the large chirp rate can be achieved by EOM being driven by an amplified output of a VCO (voltage controlled oscillator) modulated with a sawtooth input voltage [44].

Here we propose a frequency-chirped laser slowing scheme based on two EOMs. They are used to compensate the rapidly changing Doppler shifts arised from the slowing via a positive first-order sideband, and to cover the hyperfine energy structure, respectively. Unlike the atomic case, the slowing transition for molecules is usually chosen to eliminate rotational branching, where the rotational quantum number N' of the excited state is less than that of the ground state. This introduces type-II systems ($F' = F$ or $F-1$) and makes type-II transition inevitable, where F is total angular momentum quantum number and the prime indicates the excited state [45]. Consequently dark Zeeman sublevels are introduced and must be destabilized to keep the transition cycling going, which is solved by applying a magnetic field here. In addition, we find that for a specific light field, there is an optimal magnetic field to maximize the scattering rate [34]. However, there is a large difference both in spectrum distribution as well as the laser intensity during a whole slowing sequence. This is because all EOM-modulated light components are concentrated on the beginning of the frequency-chirped process, and only the positive first order sideband of EOM_1-modulated light is resonant with the slow molecules in the end. As a result, we need to get a global optimal magnetic field intensity since it is a crucial factor in our scheme. By contrast, the magnetic field is not that sensitive in other molecular slowing experiments because of the light frequency being directly chirped, without such a difference in light field.

With this in mind, we carefully calculated the scattering rate maps under different magnetic field intensities based on an optical Bloch equation (OBE) model and each molecule trajectory is simulated by a semi-classical Monte-Carlo approach. With the optimization of a large parameter space, the number of a slowed MgF beam satisfying a typical MOT-loading metric is possible to achieve $\sim 1.4\times10^6$–10^7 with a slowed peak longitude speed of 10 m/s, which is promising to a better implementation of MOT. In the following, we will show the details of our scheme in Section 2. Then, in Section 3, we present the specific approach for simulation and in Section 4 we numerically simulate the three-dimensional deceleration of MgF molecules, focusing on the influence of modulation configuration of EOM as well as the magnetic field on the slowing results.

2 Scheme for frequency-chirped laser slowing of MgF

2.1 Level structure of MgF

Figure 1(a) shows the vibrational energy structure of MgF and corresponding branching ratios between them [46, 47]. The laser denoted by $\mathcal{L}_{vv'}$ drives the $X^2\Sigma^+(v) \rightarrow A^2\Pi_{1/2}(v')$ transition. $\mathcal{L}_{00}$ is the main slowing light with wavelength $\lambda_{00} = 359.3$ nm and natural linewidth $\Gamma = 2\pi\times22$ MHz. During the optical slowing cycle, molecules leaks to $X^2\Sigma^+(1)$ and then the population accumulating in this vibrational state is repumped back via the $\mathcal{L}_{10}$ repumping light, the wavelength of which is $\lambda_{10} = 368.7$ nm. Figure 1(b) illustrates the hyperfine structure of MgF. The $X^2\Sigma^+(v=0, N=1)$ state splits into $F = 1^-, 0, 1^+, 2$ because of the spin–rotation interaction and nuclear spin, and energy intervals are 109.7, 120.3 and 9.2 MHz, respectively. In order to cover the hyperfine structure, the $\mathcal{L}_{00}$ light needs to be modulated by an EOM to generate sidebands, as well as the $\mathcal{L}_{10}$ light.

2.2 Scheme

As shown in Fig. 2(a), the main slowing light and the repumping light pass through EOM_1 and EOM_2, successively. They are used to chirp frequency and cover hyperfine structure, respectively. In order to compensate the Doppler shifts the modulation frequency f_{m1} is continuously changed via EOM_1 being driven by an amplified output of a VCO modulated with a sawtooth input voltage. And the chirping rate can be precisely controled. Note that the chirp rate applied to the repumping light should be multiplied by a factor of $\lambda_{00}/\lambda_{10}$. A pulsed beam of MgF is produced by a cryogenic buffer

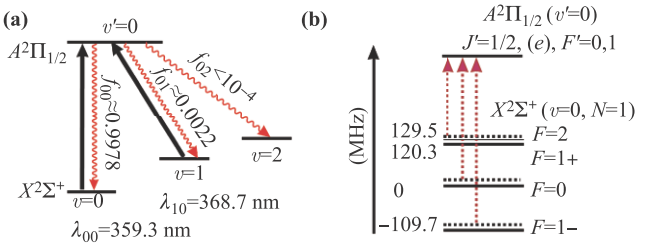

Fig. 1 The energy structure of MgF. **(a)** Relevant vibrational levels structure and branching ratios of the $X^2\Sigma^+(v) \rightarrow A^2\Pi_{1/2}(v')$ transition. Upward solid lines denote transitions driven by lasers $\mathcal{L}_{vv'}$ in practice. Spontaneous decays from the $A^2\Pi_{1/2}(v')$ state (solid Wavy line) are governed by the vibrational branching fractions, which is denoted by $f_{v'v}$. **(b)** Relevant rotational energy levels, splittings, and pumping configuration. The multi-frequency configuration of $\mathcal{L}_{00}$ that arises from the modulation is denoted by dashed line and dashed arrow.

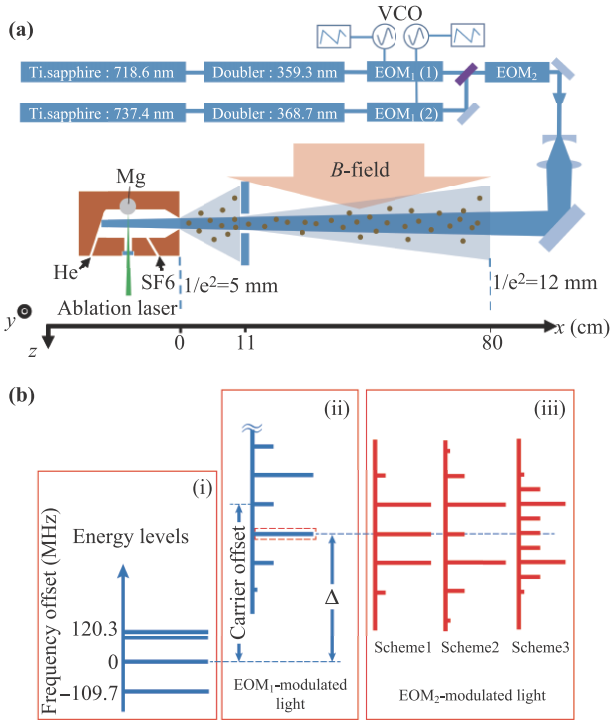

Fig. 2 Scheme of frequency-chirped laser slowing. As shown in **(a)**, the main slowing light λ_{00} and repumping light λ_{10} are frequency modulated by $\mathrm{EOM}_1(1)$, $\mathrm{EOM}_1(2)$, passing through EOM_2, and then directed at the nozzle of a buffer gas chamber after lights being expanded and focused. Magnetic filed B is used to remix dark Zeeman levels. Purple mirror is dichroscope and gray mirrors are high-reflector and lens. **(b)** Modulation configuration of EOM_1 and EOM_2. (i) Relevant energy levels. (ii) EOM_1-modulated light. A modulation depth γ_1 of 1.84 rad is applied to EOM_1 and the modulation frequency f_{m1} is varied by the input RF (radio frequency) signal. The carrier offset is fixed to compensate the Doppler shift at the beginning of the slowing period. The frequency component in red dotted frame is the positive first-order sideband. Δ is the detuning from the positive first-order sideband to the $F = 0 \rightarrow F' = 0, 1$ transition. (iii) EOM_2-modulated light. To simplify, only the EOM_2-modulated frequency components of the positive first-order sideband in (ii) is depicted. Scheme 1: $\gamma_2 = 1.43$ rad, $f_{m2} = 115$ MHz. Scheme 2: $\gamma_2 = 1.84$ rad, $f_{m2} = 115$ MHz. Scheme 3: $\gamma_2 = 3.03$ rad, $f_{m2} = 57.5$ MHz.

gas source [48–50], and they exit the cell at $x = 0$ mm via a 5 mm diameter aperture. The main slowing light and the repumping one counter-propagate to the molecular beam, being expanded and then focused to converge the lights with a $1/e^2$ diameter d of 5 mm at $x = 0$ mm and 12 mm at $x = 800$ mm. Such light bunching is helpful to reduce transverse divergence [37]. In practice, there is laser power of ~ 1 W in both $\mathcal{L}_{00}$ and $\mathcal{L}_{10}$. After considering the transmission losses from the optical surfaces, the actual light intensity used for slowing can reach 600–700 mW. So the maximum total saturation parameter $S_{\max} = I_0/I_{sat}$, where $I_0 = 2P/[\pi(d/2)^2]$ and $I_{sat} = \pi hc\Gamma/(3\lambda^3) = 62.5$ mW/cm^2, used in the simulation is ~ 100. The two wavelength components are linearly polarized, both at 60° to a uniform magnetic field directed along z, which prevents optical pumping into dark Zeeman sublevels [34, 51, 52].

As shown in Fig. 2(b)ii, the initial carrier offset (overall detuning), which is fixed for a specific initial central forward speed, is chosen so that molecules near the peak of the velocity distribution are Doppler shifted into resonance. In addition, the positive first-order sideband is what we concern because it is needed to continuously resonate with the molecules during slowing. As a result, a modulation depth γ_1 of 1.84 rad is applied to EOM_1, such that 34% of the laser beam power is contained in each first-order sideband. This setup is fixed throughout the paper. For EOM_2, we fixed the modulation frequency f_{m2} at 115 MHz or 57.5 MHz under different modulation depth, which involves three modulation configurations, shown in Fig. 2(b)iii. And the corresponding analysises are shown in Section 4.1.

3 Approach for simulation

Simulations are useful to evaluate the performance of our slowing scheme and many variable parameters need to be optimized, such as chirp rate, the magnitude of applied magnetic field, as well as the modulation configurations of EOM_1 and EOM_2. Based on the OBE model, a semi-classical Monte Carlo approach is used to simulate individual molecule trajectories. The OBE model is found to accurately agree with most observed experiment results [28, 33, 34]. In our model we consider 12+1 ground states marked as g_m $(m = 1, 2, \cdots, 13)$ and four excited states marked as e_n $(n = 1, 2, 3, 4)$ in the MgF molecule. The ground states contain 12 Zeeman sublevels in the $X^2\Sigma^+$ $(v = 0, N = 1)$ states and another one state includes all other possible levels as the total population probability is equal to 1. The total Hamiltonian is $H = H_0 + H_{int} + H_{Zeeman}$, where H_0 is the zero-field energy, H_{Zeeman} is the Hamiltonian related to energy shift under a magnetic field and H_{int} is the interaction between the system and the light field. H_{int} can be expressed by $-\hat{d} \cdot \boldsymbol{E}$, where $\hat{d}$ is the electric-dipole operator, and an arbitrary multi-frequency light field $\boldsymbol{E}$ can be decomposed as

$$\boldsymbol{E} = \sum_{nq} \frac{1}{2} |E_n| G_n^q \hat{\epsilon}_q \mathrm{e}^{\mathrm{i}\boldsymbol{k}\cdot\boldsymbol{r}} \mathrm{e}^{-\mathrm{i}\omega_n t} + \mathrm{c.c}, \tag{1}$$

where n is the frequency component index and $q = 0, \pm 1$, corresponding to the $\pi, \sigma^{\pm}$ transition. If the magnetic field is along the z axis (quantization axis), $\hat{\epsilon}_q$ under the Cartesian coordinate axis are $\hat{\epsilon}_0 = \hat{z}$ and $\hat{\epsilon}_{\pm 1} = \mp 1/\sqrt{2}(\hat{x} + \hat{y})$. And G_n^q is derived by projecting the polarization vectors of n-th frequency component on these basic ones. Then combined with $\Omega_n = d|E_n|/\hbar$, the H_{int} Hamiltonian can

expressed by

$$H_{int} = \hbar \sum_{n,q,e,g} \Omega_{ge}^{nq} |g\rangle \langle e| + \text{h.c.}, \tag{2}$$

and,

$$\Omega_{ge}^{nq} = -\frac{1}{2} r_{ge}^{q} G_{n}^{q} \mathrm{e}^{\mathrm{i}\boldsymbol{k}\cdot\boldsymbol{r}} \mathrm{e}^{-\mathrm{i}\omega_n t} \Omega_n, \tag{3}$$

where $r_{ge}^{q} = r_{ge} \cdot \hat{\epsilon}_q$ are the relative electric-dipole transition matrix elements for all electric dipole allowed transitions, and Ω_n can also be written as $\Gamma\sqrt{S/2}$. Using Eqs. (2) and (3), the model equations can be written as

$$\dot{\rho} = \frac{1}{\mathrm{i}\hbar} [H, \rho] + L(\rho), \tag{4}$$

where $L(\rho)$ is the Linblad operator to account for spontaneous decay. For the multilevel system, $L(\rho)$ is written as

$$L(\rho) = -\frac{1}{2} \sum_{ge} \left(C_{ge}^{\dagger} C_{ge} \rho + \rho C_{ge}^{\dagger} C_{ge} \right) + \sum_{ge} C_{ge} \rho C_{ge}^{\dagger}, \tag{5}$$

where

$$C_{ge} = \sqrt{\Gamma_{ge}^{q}} |g\rangle \langle e| \tag{6}$$

with the decay rate $\Gamma_{ge}^{q} = \Gamma \cdot |r_{ge}^{q}|^2$ from $|e\rangle$ to $|g\rangle$. In the calculation, the equations are dimensionless and a rotational wave approximation is used to improve calculation efficiency.

The simulation starts with randomly generating a set of molecules with initial velocity and position in three-dimensional space according to a normal distribution. Each trajectory is calculated as follows. At each time step dt the probability of scattering a photon is $P = R_{sc} \mathrm{d}t$ [53]. The scattering rate

$$\overline{R}_{sc} = \sum_{i} \frac{1}{T} \int_{0}^{\mathrm{T}} \rho_{e_i e_i}(t) \Gamma \mathrm{d}t, \tag{7}$$

is an average over a period time that enables the steady state to be reached, where $\rho_{ee}(t)$ is the transient population of excited states, and the sum is over all excited states and $T = 700\tau$ ($\tau = 7.2$ ns). The scattering rates calculated from Eq. (7) are sufficient because the populations reach the steady state on a timescale that is much shorter than any changes in the slowing parameters. The calculated scattering rate here is about the order of 10^6–10^7 photons/s. The time step is chosen 1×10^{-8} s here so that $P \ll 1$. A random number r is chosen between 0 and 1. If $P > r$ a photon is scattered [53]. Once the scattering event happens, the momentum of molecule in the direction of light's k vector is increased by $\hbar k$ to account for the absorption, which is followed by the momentum in a direction chosen at random from an isotropic distribution being increased by $\hbar k$ to account for spontaneous emission.

In the simulation, the position and velocity of molecules vary after each time step, which results in the change of light intensity and detuning that molecules feel. So a scattering rate map $R_{sc}(\Delta, S)$ is needed to address a large range of detuning Δ and saturation parameter S values once the frequency spectrum and polarization of the light are fixed. It is made by sufficiently calculating R_{sc} for a set of Δ and S, then interpolating over these values.

4 Results

A free flight and deceleration process are involved in a complete slowing sequence. After slowing finished, molecules arrive at $x = 800$ mm, where there is a detector as well as the position of an MOT. In addition, only molecules passing within a 10 mm diameter circle centered on the z axis are counted there. Such setup is reasonable because trapping force approximately peaks at a displacement of 10 mm in a typical molecular MOT, being sufficient to load a molecular beam with a diameter of 10 mm. Also, a typical range of capture velocity in an MOT is up to $\sim$ 20 m/s and peaks at $\sim$ 10 m/s [35, 37]. For a metric to compare the simulation results, we choose the total number of slowed molecules whose speed distribution is range from 0 m/s to 20 m/s, which is maximized under the condition of satisfying a typical MOT-loading metric.

A complete numerical optimization consists of the MOT position, convergence, initial carrier offset, free flight time, deceleration time, chirp rate, modulation configuration of EOM_2, applied magnetic field and laser power. However, that involves too large a parameter space to be practical. Instead, we fixed the convergence, MOT position, total laser power and the modulation depth of EOM_1 as mentioned above to reduce the dimension of the parameter space.

4.1 Optimization of the modulation configuration of EOM_2

As stated in Section 2.2, the positive first-order sideband is required to continuously resonant with molecules. In order to simplify and focus on the optimization of the modulation configuration of EOM_2, we only consider the contribution of the positive first-order sideband of the EOM_1-modulated light to each scattering rate map. Since the total saturation parameter $S_{\max}$ is $\sim$ 100 and $\gamma_1 = 1.84$ rad, the maximum S of the positive first-order sideband of the EOM_1-modulated light is $\sim$ 34. The magnetic field applied here is 15 G.

There are three modulation configurations for EOM_2

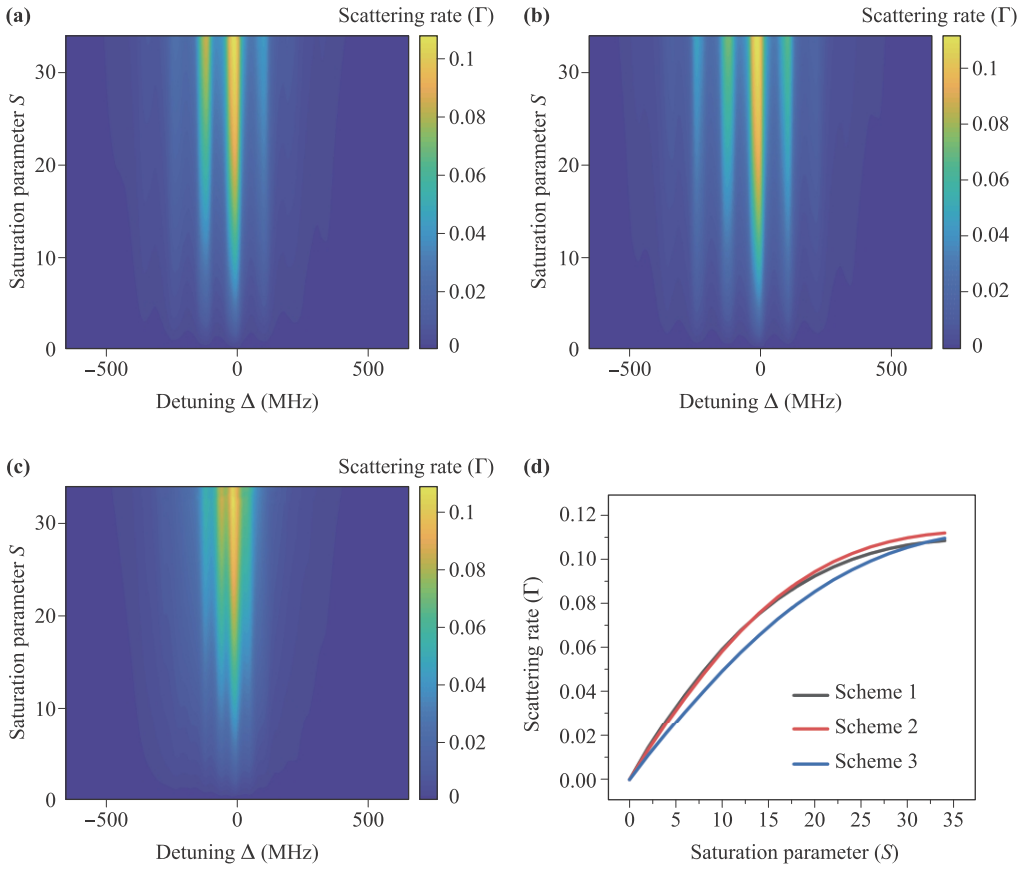

Fig. 3 Scattering rate under different modulation configurations of EOM_2. The detuning Δ is the frequency offset from the carrier wave to the transition of $F = 0 \rightarrow F' = 0, 1$. Scattering rate maps versus detuning Δ and saturation parameter S are depicted under **(a)** Scheme 1, **(b)** Scheme 2 and **(c)** Scheme 3. **(d)** The peak scattering rate of three schemes versus saturation parameter S. The detuning Δ is near zero.

here, whose specific parameters are shown in the caption of Fig. 2. The corresponding distribution of laser power under different modulation depth is listed in Table 1. Figure 3 shows the scattering rate map of three modulation configurations, and the peak scattering rate in each scheme is depicted Fig. 3(d). We found that the peak scattering rate in Scheme 2 is the largest when the maximum S is about 34. More laser power are contained in the negative first-order sideband of EOM_2-modulated light addressing the population in $F = 1^+, 2$ states in that case. At the same time, considering the condition that the $F = 0$ state is addressed by much less laser power in Scheme 2 than in Scheme 1, we regard the excitation of $F = 1^+, 2$ states as a more important contribution to the scattering rate. Although the usage of EOM_2 is to achieve an optimal coverage of hyperfine structure rather than address molecules with many different speeds, Scheme 3 is an attempt to balance these two ambitions. As shown in Fig. 3(d), the peak scattering rate in Scheme 3 is apparently smaller but it is similar to that in Scheme 1 under the circumstance of $S = 34$ resulting from the power broadening.

During the optimization, the output from a buffer gas source is assumed to have a forward velocity distribution centered at 200 m/s with a full width at half maximum (FWHM) of 100 m/s [33, 53], and the FWHM of transverse velocity distribution is fixed at 2 m/s after molecules passing through the collimation hole [14]. And initial transverse positions are chosen from a Gaussian distribution of 4 mm FWHM, corresponding to the 5 mm diameter exit aperture of the cell. A single-photon recoil velocity for MgF is 2.56 cm/s, which indicates that the molecule with a forward velocity of 200 m/s will be brought to rest after scattering $\sim$ 7800 photons. The initial central forward velocities of 100 and 300 m/s are also involved in

Table 1 Percentage of each modulated frequency component in total laser power under different modulation depth of EOM.

	Modulation depth (rad)		
	1.43	1.84	3.03
Carrier wave	30%	10%	9.9%
First-order sideband	30%	34%	9.9%
Second-order sideband	4.6%	10%	23%
Third-order sideband	0.3%	1%	9.8%

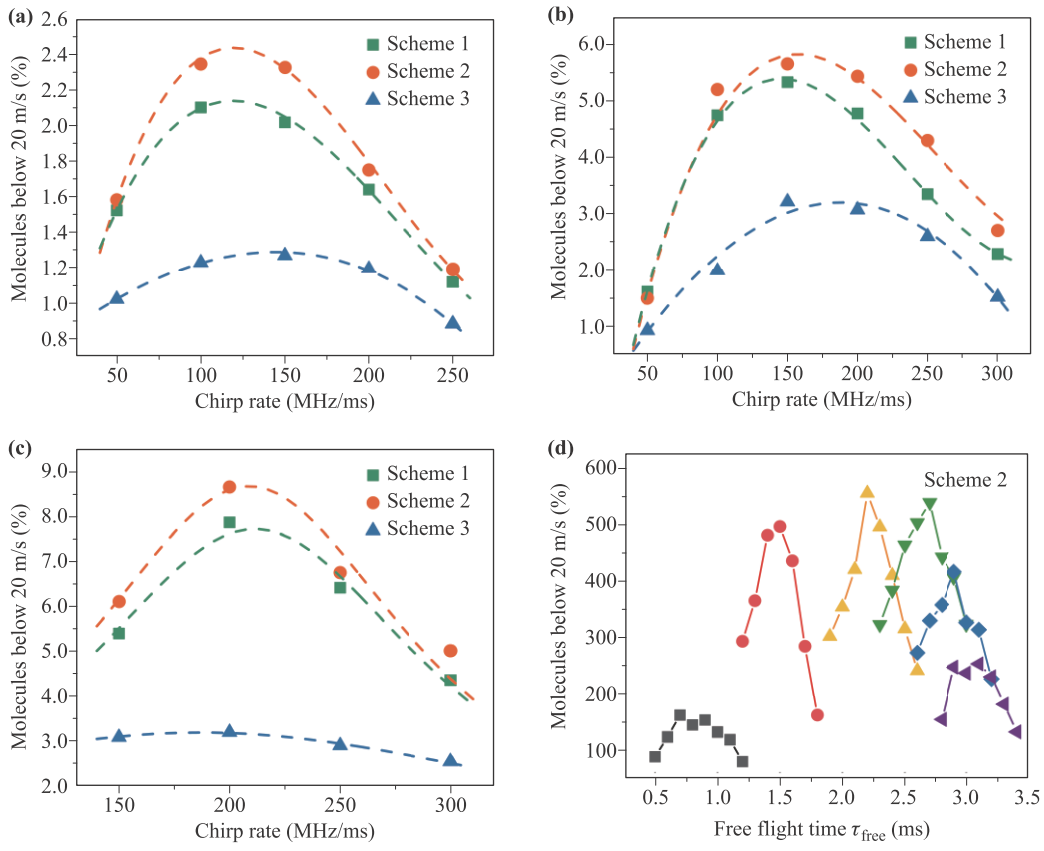

Fig. 4 Comparison of slowing results in different modulation configurations of EOM_2. Number of molecules satisfying the MOT-loading metric versus chirp rate β with initial central forward velocity $v_i = 100$ m/s **(a)**, 200 m/s **(b)** and 300 m/s **(c)**. The dashed lines are the fitting curves. **(d)** Scheme 2, $v_i = 200$ m/s. The deceleration time τ_{dec} is fixed at 7.6, 4.9, 3.3, 2.5, 2.05 and 1.72 ms for chirp rate from 50 MHz/ms to 300 MHz/ms respectively, shown from left to right. In all plots, the spread of forward and transverse velocity are 100 m/s and 2 m/s.

the optimization of EOM_2 modulation configuration for integrity.

The corresponding results are shown in Fig. 4, where all the plots in (a), (b) and (c) are optimized as depicted in (d). A deceleration time is chosen so that the slowed molecules peaks at 10 m/s when they arrive the position of an MOT, and the free flight time is slightly varied to maximize the number of molecules below 20 m/s after fixing the deceleration one. The corresponding parameters used in Fig. 4(d) are listed in the caption. It is obvious that the number of molecules satisfying the MOT-loading metric in Schemes 1 and 2 is much more than that in Scheme 3 upon most occasions. And as expected, the larger scattering rate in Scheme 2 has a better performance on slowing results. Another interesting phenomenon is that the overall optimal chirp rate for each Scheme is gradually shifted to a larger value with faster initial central forward speed. This can be explained as follows. For faster molecules, a longer deceleration time results in a shorter free flight time once the MOT position is fixed. The shorter the free flight time, the more significant the inhibition on the transverse dispersion of the molecular beam due to the convergence of slowing light. This brings molecules to interact with the light of greater intensity since they are more close to the center of the light beam, which results in chirping frequency faster to meet the larger scattering rate.

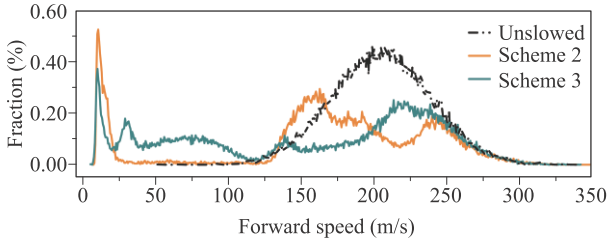

Fig. 5 Forward velocity distribution of slowed and unslowed molecules. The dashed line indicates the unslowed distribution, and the slowing results of Scheme 2 and Scheme 3 are ploted in orange and green line respectively. For Scheme 2, slowing start time $t_{start} = 2.3$ ms and the deceleration time $\tau_{dec} = 3.3$ ms. For Scheme 3, $t_{start} = 2.25$ ms and $\tau_{dec} = 3.35$ ms. For both cases, $v_i = 200$ m/s and chirp rate is 150 MHz/ms.

Figure 5 shows the forward velocity distribution of slowed and unslowed molecules. Obviously that in Scheme 2 there still has a velocity distribution of the central speed at around 160 m/s other than the molecules satisfying the MOT-loading metric. The molecules of this portion are out of resonance with slowing light. However, the situa-

tion is improved in Scheme 3. It seems like the attempt to address molecules with many different speeds is effective by using EOM_2 modulated with Scheme 3, but the lower scattering rate results in a less number of molecules satisfying the MOT-loading metric when the laser power is not that strong. So we choose Scheme 2 for the following optimization.

4.2 Optimization of applied magnetic field with all light components considered

After fixing the modulation configuration of EOM_2 in the way of Scheme 2, we considering the contribution of all the sidebands components of EOM_1-modulated light to scattering rate maps. At the beginning of frequency chirping, all the laser power ($S = \sim 100$) concentrates over a very small frequency range, and a white-light-like slowing is formed but it lasts a short time. Almost all the molecules are slowed at this stage. However, as the f_{m1} gradually increases, the gaps between the frequency components become larger. Thus the frequency-chirped slowing is dominant in the residual process of a slowing sequence, where almost all the sidebands components of EOM_1-modulated light are out of resonance with the molecules of target forward speed except the positive first-order sideband ($S = \sim 34$ if the total saturation parameter is ~ 100).

The magnetic field applied to remix dark Zeeman sublevels is a crucial factor to slowing efficiency η, and there is an optimum range of magnetic field strength for the laser field, shown in both the theoretical calculation [51] and the experiments [54]. If the magnetic-field strength is too small, molecules in a dark state do not evolve into a bright state very quickly. If the strength is too large, the scattering rate will be decreased again because the molecules may precess back to the dark state before optical pumping can occur. Also, the Zeeman shifts are too large to resonant with. The corresponding conclusion can be found in our previous work of the destabilization of dark states in MgF molecules [34], where the experiment and theory are in good agreement. Since there are two stages during a whole slowing sequence, the overall slowing efficiency is dependent on a balance of the scattering rate between the white-light-like slowing stage and frequency-chirped slowing one. In other words, the optimum magnetic field strength that suits the previous stage is not directly applicable to the latter one. To get the global optimal magnetic field, we calculate the scattering rate maps in the cases of several magnetic field intensities and compare the slowing results upon each case. In addition, the rate maps vary with different f_{m1} values and they are needed to be re-calculated separately. In our simulation, the maps are calculated at f_{m1} of every 2 MHz interval for each case in advance, which is sufficient because the interval is much smaller than the natural linewidth. The map that best fits the current light field distribution is selected at every time step during a single simulation.

The above scattering rate maps are shown in Fig. 6.

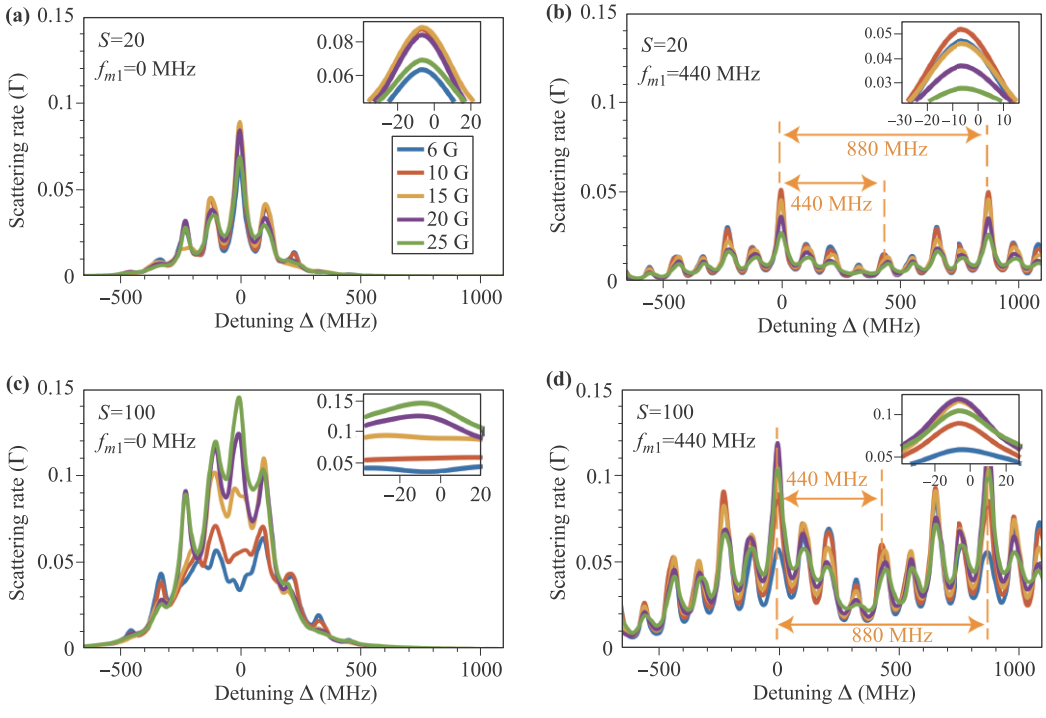

Fig. 6 Scattering rate under different magnitudes of magnetic field applied. The detuning Δ is the frequency offset from the positive first-order FM sideband of the EOM_1-modulated light to the $F = 0 \rightarrow F' = 0, 1$ transition. For all plots, $\gamma_1, \gamma_2 = 1.84$ rad and $f_{m2} = 115$ MHz. The scattering rate of $B = 6$ to 25 G are shown in blue, red, yellow, purple and green lines respectively. The insets are near-resonance scattering rates. The curve color in **(b–d)** is the same as that in **(a)**.

The total saturation parameters in the first and second rows are $S = 20$ and 100, respectively. And the f_{m1} values in the first and second column are 0 and 440 MHz, respectively. In Figs. 6(a) and (c), when $f_{m1} = 0$ MHz, all EOM_1-modulated light components are concentrated on the frequency of the carrier wave and the scattering rate will have several peaks in the range of 600 MHz resulting from the modulation of EOM_2. When $f_{m1} > 0$, a compound modulation configuration is formed and each EOM_1-modulated light component will have a multi-frequency structure, whose center is respectively separated by f_{m1}. As shown in Figs. 6(b) and (d), when $f_{m1} = 440$ MHz, there are the intervals of 440 and 880 MHz between a first-order sideband of EOM_1-modulated light and the carrier wave, and between two first-order sidebands, respectively. Also, it is obvious that for nearly all f_{m1} values the scattering rate in the case of a stronger magnetic field is smaller than that in the case of a weaker magnetic field when the laser power is low, shown in the insets of Figs. 6(a) and (b). However the situation reverses if the laser power is strong, shown in the insets of Figs. 6(c) and (d). In addition, the peak scattering rate varies by ~ 3 times in the inset of (c) among different magnetic fields and thus such a big difference cannot be neglected in our scheme.

The corresponding slowing results are shown in Fig. 7. The relationship between chirp rate and slowing efficiency of each magnetic case is ploted in (a). Although the scattering rate is large in strong magnetic field when laser power is high, molecules only spend little time interacting with the strong light during a whole slowing sequence. When they are slowed close to the MOT position, $1/e^2$ diameters of lights become larger. Also, they further away from the light axis due to the transverse heating as well as the divergence. These two factors will weaken the light intensity the molecules feel. Consequently, larger magnetic field is not a good choice for slowing efficiency. However a weak magnetic field cannot satisfy a required Larmor precession frequency in the case of high laser power. We suggest that a magnetic of ~ 10 G can well balance the scattering rate in both cases [Fig. 7(a)]. For example, when $B = 10$ G and chirp rate is 250 MHz/ms, the free flight time and deceleration time are 2.8 and 2.02 ms respectively. About 7420 photons are scattered in 2.02 ms and an average scattering rate of 3.67×10^6 photons/s is obtained. The range of f_{m1} is from 0 to 505 MHz.

Notice that there is a slowly rising part of curve in each magnetic field case, because in this region there is a competition between the positive second-order sideband with a faster chirp rate as well as a weaker light intensity and the positive first-order sideband with a slower chirp rate as well as a stronger light intensity. When B

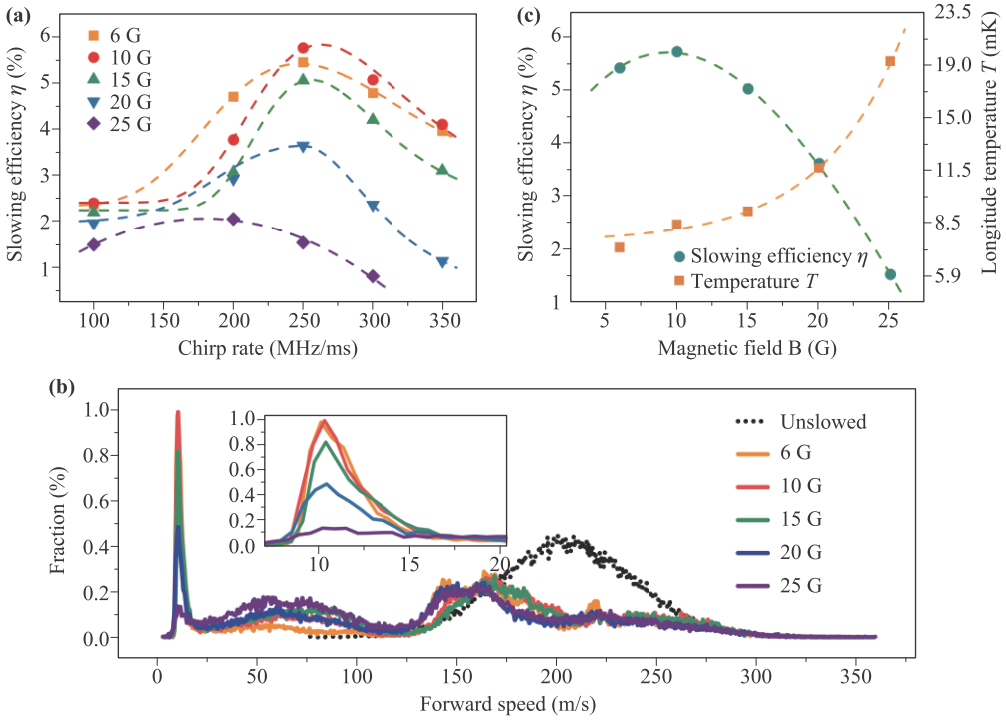

Fig. 7 Comparison of slowing effects in different magnetic field. **(a)** Slowing efficiency η versus chirp rate β in different magnetic field. Slowing efficiency is the fraction of molecules satisfying the MOT-loading metric. **(b)** The forward speed distribution in different magnetic field with optimized parameter. **(c)** The slowing efficiency η and corresponding longitude temperature versus magnetic field B. In all plots, the spread of forward and transverse velocity is 100 m/s and 2 m/s. All dashed lines in (a) and (c) are the fitting curves.

= 10 G and β = 100 MHz/ms, the second-order sideband has a doubled chirp rate with a deceleration time of 2.56 ms, performing better than the first-order sideband with a deceleration time of 5.07 ms. However when $\beta = 200$ MHz/ms, the first-order sideband with a deceleration time of 2.52 ms results in a better slowing efficiency. And we only depicted the better results for each chirp rate in (a). Only when the first order sideband is chirped with an optimal rate, can the slowing efficiency reach the maximum, which is around 250 MHz/ms. If the chirp rate is larger, the slowing efficiency is quickly decreased again because of the Doppler shifts being out of sync.

Figure 7(b) shows the forward speed distribution of each magnetic field case. The dotted line is the initial forward speed distribution. Since there is a white-light-like slowing stage at the beginning, almost all the molecules are slowed, and especially those that is continuously resonant with the chirped frequency are slowed down below 20 m/s. The inset of Fig. 7(b) shows the detailed distribution over a small speed range. It is clear that the distribution of each case is peaks at 10 m/s and the corresponding FWHM is narrow, indicating that the longitude temperature is very low after molecules slowed. However, a bunch of molecules in the range of 150–200 m/s are lost in the slowing sequence. To solve the problem, one possible method is to increase the laser power and modulate EOM_2 with Scheme 3. Scheme 3 can well address molecules with different speed and the increased laser power might improve the relatively low scattering rate. Another method is to combine transverse cooling with the slowing. They are out of sync because they feel the less scattering rate than expectation. The narrowed divergence of the molecular flux after transverse cooling can help them meet the stronger laser since the light intensity is Gaussian distribution. Consequently, they will gain the expected scattering rate to sync with the chirping frequency.

The temperature can be derived from $T = m(\delta v)^2/(8k_B \ln 2)$, where m is the mass, δv is the FWHM of speed distribution, and k_B is the Boltzmann constant. Although the longitude temperature of the slowed molecules in the case of $B = 6$ G is lower than that in the case of $B = 10$ G, the slowing efficiency of the latter case is better, which is shown in (c). The range of slowing efficiency and longitude temperature are 1.7%–5.7% and 7.8–20 mK respectively. When B = 10 G and β = 250 MHz/ms, the slowing efficiency is 5.7% with the longitude and transverse temperature of 9 and 2.1 mK. In the case of $B > 10$ G , the slowing efficiency decreases as the longitude temperature increases. Since the main loss mechanism is the natural increase in divergence of slower molecules, the large scattering rate in the white-light-like slowing stage results in most molecules being slowed down too early to sync with chirp stage. Then they travel a longer time with the divergence, further away from the light axis. Although those molecules are resonant with the chirped frequency later, the weak scattering rate resulting from the weaker light

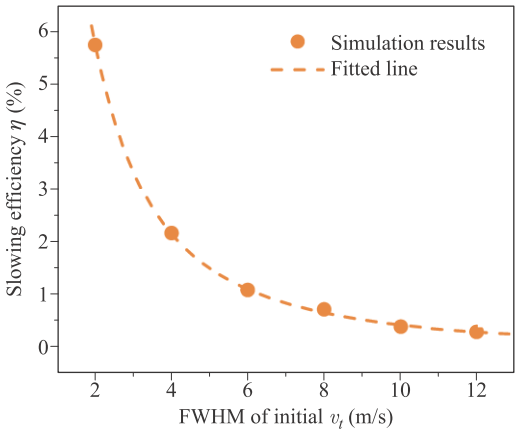

Fig. 8 The slowing efficiency η versus different FWHM of initial transverse speed v_t. The else parameters are: v_i = 200 m/s, the spread of forward speed is 100 m/s, B = 10 G, chirp rate is 250 MHz/ms, the free flight time and deceleration time is 2.8 and 2.02 ms.

makes the effect of the chirp stage insignificant. Thus molecules are slowed with a worse efficiency and higher temperature in a large magnetic field B.

So far, we have optimized the slowing scheme with a large parameter space, especially the modulation configuration and the magnetic field applied. And the optimal slowing efficiency is 5.7% when the initial FWHM of transverse speed distribution is 2 m/s. In order to get such a distribution, a 1.5 mm × 1.5 mm aperture is placed at z = 110 mm further collimating the molecular beam, which results in a steradian of 1.9×10^{-4} [14]. If the flux of MgF from a buffer gas chamber is 2×10^{11}–10^{12} per steradian per molecular pulse in the X ($v = 0, N = 1$) state [33, 37], the slowed MgF molecules satisfying a typical MOT-loading metric are estimated by 1.4×10^6–10^7. In addition, the divergence of a molecular beam reduces the fraction of slow molecules that pass through the detection volume, which is shown in Fig. 8. The slowing efficiency is decreased from 5.7% to 0.3% as the FWHM of initial transverse distribution is increased from 2 m/s to 12 m/s.

5 Conclusion

We have shown that the MgF molecules from a cryogenic buffer-gas chamber are possible to be slowed down satisfying a typical MOT-loading metric with a good brightness in our scheme. And the influence of the modulation configuration of EOM as well as magnetic field on the slowing results are carefully discussed. We find that a modulation depth of $\gamma_1, \gamma_2 = 1.84$ rad is a good choice because the laser power of the first-order sideband of EOM_1- and EOM_2-modulated light are maximized to well compensate the Doppler shifts and address the $F = 1^+, 2$ states, respectively. A magnetic field of around 10 G can globally

balance the scattering rate during a slowing sequence, as the light field is changed with frequency chirped. If initial molecules have a Gaussian forward speed distribution centered at 200 m/s with an FWHM of 100 m/s, their central forward speed can be slowed down to 10 m/s with an FWHM of 3.08 m/s, whose longitude temperature is 9 mK. Thanks to the large natural linewidth and recoil speed, only about 7420 photons are scattered in a short deceleration time of 2.02 ms and an average scattering rate of 3.67×10^6 photons/s is obtained. When the FWHM of initial transverse speed distribution is 2 m/s, the slowing efficiency can reach 5.7% and the number of molecules satisfying a typical MOT-loading metric is estimated by 1.4×10^6–10^7 considering the yield from a buffer-gas source as well as a divergence angle. Combined with the loss of MOT-loading, about 2×10^5–10^6 MgF molecules are possible to be confined in an MOT. In addition, the slowing efficiency can be furtherly improved by using a transverse cooling. The discussion presented here provides a suitable laser cooling scheme for fast frequency-chirped case in a type-II transition cycling and a general optimizing method to improve the slowing results combined with a magnetic field applied.

Acknowledgements Financial supports are from the National Natural Science Foundation of China under Grant Nos. 11834003, 91836103, and 91536218.

References

1. J. Doyle, B. Friedrich, R. V. Krems, and F. Masnou-Seeuws, Editorial: Quo vadis, cold molecules? *Eur. Phys. J. D* 31(2), 149 (2004)
2. L. D. Carr, D. DeMille, R. V. Krems, and J. Ye, Cold and ultracold molecules: Science, technology and applications, *New J. Phys.* 11(5), 055049 (2009)
3. The ACME Collaboration, J. Baron, W. C. Campbell, D. DeMille, J. M. Doyle, G. Gabrielse, Y. V. Gurevich, P. W. Hess, N. R. Hutzler, E. Kirilov, I. Kozyryev, B. R. O'Leary, C. D. Panda, M. F. Parsons, E. S. Petrik, B. Spaun, A. C. Vutha, and A. D. West, Order of magnitude smaller limit on the electric dipole moment of the electron, *Science* 343(6168), 269 (2014)
4. J. J. Hudson, D. M. Kara, I. J. Smallman, B. E. Sauer, M. R. Tarbutt, and E. A. Hinds, Improved measurement of the shape of the electron, *Nature* 473(7348), 493 (2011)
5. S. Ospelkaus, K. K. Ni, D. Wang, M. H. G. De Miranda, B. Neyenhuis, G. Quéméner, P. S. Julienne, J. L. Bohn, D. S. Jin, and J. Ye, Quantum-state controlled chemical reactions of ultracold potassium–rubidium molecules, *Science* 327(5967), 853 (2010)
6. D. S. Jin and J. Ye, Introduction to ultracold molecules: New frontiers in quantum and chemical physics, *Chem. Rev.* 112(9), 4801 (2012)
7. D. DeMille, Quantum computation with trapped polar molecules, *Phys. Rev. Lett.* 88(6), 067901 (2002)
8. A. André, D. DeMille, J. M. Doyle, M. D. Lukin, S. E. Maxwell, P. Rabl, R. J. Schoelkopf, and P. Zoller, A coherent all-electrical interface between polar molecules and mesoscopic superconducting resonators, *Nat. Phys.* 2(9), 636 (2006)
9. P. Rabl, D. DeMille, J. M. Doyle, M. D. Lukin, R. J. Schoelkopf, and P. Zoller, Hybrid quantum processors: Molecular ensembles as quantum memory for solid state circuits, *Phys. Rev. Lett.* 97(3), 033003 (2006)
10. A. Micheli, G. K. Brennen, and P. Zoller, A toolbox for lattice-spin models with polar molecules, *Nat. Phys.* 2(5), 341 (2006)
11. D. Wang, M. D. Lukin, and E. Demler, Quantum fluids of self-assembled chains of polar molecules, *Phys. Rev. Lett.* 97(18), 180413 (2006)
12. B. Yan, S. A. Moses, B. Gadway, J. P. Covey, K. R. A. Hazzard, A. M. Rey, D. S. Jin, and J. Ye, Observation of dipolar spin-exchange interactions with lattice-confined polar molecules, *Nature* 501(7468), 521 (2013)
13. Y. Liu and L. Luo, Molecular collisions: From near-cold to ultra-cold, *Front. Phys.* 16(4), 42300 (2021)
14. E. S. Shuman, J. F. Barry, and D. DeMille, Laser cooling of a diatomic molecule, *Nature* 467(7317), 820 (2010)
15. E. B. Norrgard, D. J. McCarron, M. H. Steinecker, M. R. Tarbutt, and D. DeMille, Submillikelvin dipolar molecules in a radio-frequency magneto-optical trap, *Phys. Rev. Lett.* 116(6), 063004 (2016)
16. M. T. Hummon, M. Yeo, B. K. Stuhl, A. L. Collopy, Y. Xia, and J. Ye, 2D magneto-optical trapping of diatomic molecules, *Phys. Rev. Lett.* 110(14), 143001 (2013)
17. A. L. Collopy, S. Ding, Y. Wu, I. A. Finneran, L. Anderegg, B. L. Augenbraun, J. M. Doyle, and J. Ye, 3D magneto-optical trap of yttrium monoxide, *Phys. Rev. Lett.* 121(21), 213201 (2018)
18. L. Anderegg, B. L. Augenbraun, E. Chae, B. Hemmerling, N. R. Hutzler, A. Ravi, A. Collopy, J. Ye, W. Ketterle, and J. M. Doyle, Radio frequency magneto-optical trapping of CaF with high density, *Phys. Rev. Lett.* 119(10), 103201 (2017)
19. I. Kozyryev, L. Baum, K. Matsuda, B. L. Augenbraun, L. Anderegg, A. P. Sedlack, and J. M. Doyle, Sisyphus laser cooling of a polyatomic molecule, *Phys. Rev. Lett.* 118(17), 173201 (2017)
20. H. J. Williams, L. Caldwell, N. J. Fitch, S. Truppe, J. Rodewald, E. A. Hinds, B. E. Sauer, and M. R. Tarbutt, Magnetic trapping and coherent control of laser-cooled molecules, *Phys. Rev. Lett.* 120(16), 163201 (2018)
21. L. Anderegg, B. L. Augenbraun, Y. Bao, S. Burchesky, L. W. Cheuk, W. Ketterle, and J. M. Doyle, Laser cooling of optically trapped molecules, *Nat. Phys.* 14(9), 890 (2018)
22. S. Truppe, H. J. Williams, M. Hambach, L. Caldwell, N. J. Fitch, E. A. Hinds, B. E. Sauer, and M. R. Tarbutt, Molecules cooled below the Doppler limit, *Nat. Phys.* 13(12), 1173 (2017)
23. L. W. Cheuk, L. Anderegg, B. L. Augenbraun, Y. Bao, S. Burchesky, W. Ketterle, and J. M. Doyle, Λ-enhanced imaging of molecules in an optical trap, *Phys. Rev. Lett.* 121(8), 083201 (2018)

24. L. Caldwell, J. A. Devlin, H. J. Williams, N. J. Fitch, E. A. Hinds, B. E. Sauer, and M. R. Tarbutt, Deep laser cooling and efficient magnetic compression of molecules, *Phys. Rev. Lett.* 123(3), 033202 (2019)

25. H. Son, J. J. Park, W. Ketterle, and A. O. Jamison, Collisional cooling of ultracold molecules, *Nature* 580(7802), 197 (2020)

26. S. A. Malinovskaya, Laser cooling using adiabatic rapid passage, *Front. Phys.* 16(5), 52601 (2021)

27. Q. Liang, T. Chen, W. Bu, Y. Zhang, and B. Yan, Laser cooling with adiabatic passage for type-ii transitions, *Front. Phys.* 16(3), 32501 (2021)

28. R. L. McNally, I. Kozyryev, S. Vazquez-Carson, K. Wenz, T. Wang, and T. Zelevinsky, Optical cycling, radiative deflection and laser cooling of barium monohydride (^{138}Ba^{1}H), *New J. Phys.* 22(8), 083047 (2020)

29. J. Lim, J. R. Almond, M. A. Trigatzis, J. A. Devlin, N. J. Fitch, B. E. Sauer, M. R. Tarbutt, and E. A. Hinds, Laser cooled YbF molecules for measuring the electron's electric dipole moment, *Phys. Rev. Lett.* 120(12), 123201 (2018)

30. T. Chen, W. Bu, and B. Yan, Radiative deflection of a BaF molecular beam via optical cycling, *Phys. Rev. A* 96(5), 053401 (2017)

31. P. Aggarwal, H. L. Bethlem, A. Borschevsky, M. Denis, K. Esajas, P. A. B. Haase, Y. Hao, S. Hoekstra, K. Jungmann, T. B. Meijknecht, M. C. Mooij, R. G. E. Timmermans, W. Ubachs, L. Willmann, and A. Zapara, Measuring the electric dipole moment of the electron in BaF, *Eur. Phys. J. D* 72(11), 197 (2018)

32. R. Albrecht, M. Scharwaechter, T. Sixt, L. Hofer, and T. Langen, Buffer-gas cooling, high-resolution spectroscopy, and optical cycling of barium monofluoride molecules, *Phys. Rev. A* 101(1), 013413 (2020)

33. S. Hofsäss, M. Doppelbauer, S. C. Wright, S. Kray, B. G. Sartakov, J. Pérez-Ríos, G. Meijer, and S. Truppe, Optical cycling of AlF molecules, *New J. Phys.* 23(7), 075001 (2021)

34. M. Xia, R. Gu, K. Yan, D. Wu, L. Xu, Y. Xia, and J. Yin, Destabilization of dark states in MgF molecules, *Phys. Rev. A* 103(1), 013321 (2021)

35. M. R. Tarbutt and T. C. Steimle, Modeling magnetooptical trapping of CaF molecules, *Phys. Rev. A* 92(5), 053401 (2015)

36. H. J. Williams, S. Truppe, M. Hambach, L. Caldwell, N. J. Fitch, E. A. Hinds, B. E. Sauer, and M. R. Tarbutt, Characteristics of a magneto-optical trap of molecules, *New J. Phys.* 19(11), 113035 (2017)

37. S. Truppe, H. J. Williams, N. J. Fitch, M. Hambach, T. E. Wall, E. A. Hinds, B. E. Sauer, and M. R. Tarbutt, An intense, cold, velocity-controlled molecular beam by frequency-chirped laser slowing, *New J. Phys.* 19(2), 022001 (2017)

38. J. F. Barry, E. S. Shuman, E. B. Norrgard, and D. DeMille, Laser radiation pressure slowing of a molecular beam, *Phys. Rev. Lett.* 108(10), 103002 (2012)

39. B. Hemmerling, E. Chae, A. Ravi, L. Anderegg, G. K. Drayna, N. R. Hutzler, A. L. Collopy, J. Ye, W. Ketterle, and J. M. Doyle, Laser slowing of CaF molecules to near the capture velocity of a molecular mot, *J. Phys. B* 49(17), 174001 (2016)

40. V. Zhelyazkova, A. Cournol, T. E. Wall, A. Matsushima, J. J. Hudson, E. A. Hinds, M. R. Tarbutt, and B. E. Sauer, Laser cooling and slowing of CaF molecules, *Phys. Rev. A* 89(5), 053416 (2014)

41. M. Yeo, M. T. Hummon, A. L. Collopy, B. Yan, B. Hemmerling, E. Chae, J. M. Doyle, and J. Ye, Rotational state microwave mixing for laser cooling of complex diatomic molecules, *Phys. Rev. Lett.* 114(22), 223003 (2015)

42. M. Petzold, P. Kaebert, P. Gersema, M. Siercke, and S. Ospelkaus, A zeeman slower for diatomic molecules, *New J. Phys.* 20(4), 042001 (2018)

43. P. Kaebert, M. Stepanova, T. Poll, M. Petzold, S. Xu, M. Siercke, and S. Ospelkaus, Characterizing the zeeman slowing force for ^{40}Ca^{19}F molecules, *New J. Phys.* 23(9), 093013 (2021)

44. C. C. Bradley, J. G. Story, J. J. Tollett, J. Chen, N. W. M. Ritchie, and R. G. Hulet, Laser cooling of lithium using relay chirp cooling, *Opt. Lett.* 17(5), 349 (1992)

45. B. K. Stuhl, B. C. Sawyer, D. Wang, and J. Ye, Magnetooptical trap for polar molecules, *Phys. Rev. Lett.* 101(24), 243002 (2008)

46. L. Xu, Y. Yin, B. Wei, Y. Xia, and J. Yin, Calculation of vibrational branching ratios and hyperfine structure of ^{24}Mg^{19}F and its suitability for laser cooling and magnetooptical trapping, *Phys. Rev. A* 93(1), 013408 (2016)

47. K. Yan, B. Wei, Y. Yin, S. Xu, L. Xu, M. Xia, R. Gu, Y. Xia, and J. Yin, A new route for laser cooling and trapping of cold molecules: Intensity-gradient cooling of MgF molecules using localized hollow beams, *New J. Phys.* 22(3), 033003 (2020)

48. N. R. Hutzler, H. I. Lu, and J. M. Doyle, The buffer gas beam: An intense, cold, and slow source for atoms and molecules, *Chem. Rev.* 112(9), 4803 (2012)

49. J. F. Barry, E. S. Shuman, and D. DeMille, A bright, slow cryogenic molecular beam source for free radicals, *Phys. Chem. Chem. Phys.* 13(42), 18936 (2011)

50. N. E. Bulleid, S. M. Skoff, R. J. Hendricks, B. E. Sauer, E. A. Hinds, and M. R. Tarbutt, Characterization of a cryogenic beam source for atoms and molecules, *Phys. Chem. Chem. Phys.* 15(29), 12299 (2013)

51. D. J. Berkeland and M. G. Boshier, Destabilization of dark states and optical spectroscopy in Zeeman degenerate atomic systems, *Phys. Rev. A* 65(3), 033413 (2002)

52. E. S. Shuman, J. F. Barry, D. R. Glenn, and D. DeMille, Radiative force from optical cycling on a diatomic molecule, *Phys. Rev. Lett.* 103(22), 223001 (2009)

53. N. J. Fitch and M. R. Tarbutt, Laser cooled molecules, arXiv: 2103.00968 (2021)

54. B. Klöter, C. Weber, D. Haubrich, D. Meschede, and H. Metcalf, Laser cooling of an indium atomic beam enabled by magnetic fields, *Phys. Rev. A* 77(3), 033402 (2008)